Transactions on Additive Manufacturing Meets Medicine
Trans. AMMM, 2024, Vol. 6, No 1, Article ID 1788, 13 Pages

Infinite Science Publishing

Original Research Article

Comparison of 316L stainless steel parts produced by MEX and LPBF additive and conventional manufacturing for biomedical sensing applications

B. Schubert[1*], M. Berghaus[2], H. Apmann[2], and D. Hochmann[1]

[1] *Biomechatronics Research Laboratory, FH Münster University of Applied Sciences, Steinfurt, Germany*
[2] *Laboratory for Machine Tools and Production Engineering, FH Münster University of Applied Sciences, Steinfurt, Germany*
[*] *Corresponding author, email: bruno.schubert@fh-muenster.de*

Abstract: This study presents a comprehensive evaluation of force sensors manufactured through conventional CNC machining, laser powder bed fusion (LPBF), and material extrusion (MEX) 3D printing methods. The study utilized a combination of finite element method (FEM) simulations, functional testing, durability assessments, and ultimate strength testing in order to assess the viability of additive manufacturing for sensing technology applications. The FEM simulations provided a preliminary framework for predictive analysis, closely aligning with experimental outcomes for LPBF and conventionally manufactured sensors. Nevertheless, discrepancies were observed in the performance of MEX-printed sensors during ultimate strength testing, necessitating the implementation of more comprehensive modeling approaches that take into account the distinctive material characteristics and failure mechanisms. Functional testing confirmed the operational capability of all sensors, thereby demonstrating their suitability for the intended application. Moreover, all sensors exhibited resilience during 50,000 cycles of cyclic testing, indicating reliability, durability, and satisfactory fatigue life performance. Notably, sensors produced via LPBF exhibited a significant increase in strength, nearly three times that of conventionally manufactured sensors. These findings suggest the potential for innovative sensor design and the expansion of their use into higher-loaded applications. Overall, while both LPBF and conventional methods demonstrated reliability and closely matched simulation predictions, further research is necessary to refine modeling approaches for MEX-printed sensors and fully unlock their potential in sensing technology applications. These findings indicate that additive manufacturing of metals may be a viable alternative for the fabrication of biomedical sensors.

I. Introduction

Additive manufacturing (AM), also known as 3D printing, has become a transformative technology in various sectors, including the medical technology and medical aids industry [1,2]. The capacity to customize and rapidly produce complex structures has propelled AM to the forefront of modern manufacturing techniques [3,4]. Nevertheless, as the integration of AM in the production of critical components for the medical sector increases, ensuring that these products comply with the most stringent regulatory standards is a matter of paramount importance [5]. This necessitates the implementation of comprehensive testing and evaluation procedures to verify the reliability and performance of devices produced by additive manufacturing [6].

A critical aspect of this evaluation is the repeatability of measurement processes, which is heavily influenced by the accurate monitoring and recording of factors related to the clamping of devices in test stands [7]. Similarly, the device is fixed to the dummy in the test stand using the processed belts, in a manner analogous to its daily use. To achieve this, it is essential to quantify the forces applied to these belts using force sensors. The core component of these force

sensors is the deformable body, which is instrumented with strain gauges and deforms in response to applied loads.

The field of sensing technologies offers a diverse array of sensor types for a multitude of applications [8]. Among these, force sensing stands out as one of the most prominent and widely utilized applications within the sensing industry. Force sensors are of great value in a variety of fields, including but not limited to mechanical test benches and biomedical research and the development of various diagnostic tools. In the field of biomedical research, as well as in the broader landscape of research-oriented applications, there is often a need for customized, special sensors that are individually designed to meet the unique requirements of special test methods and complicated investigations [9]. The development of such sensors typically involves a multifaceted process, characterized by numerous iterative phases. This iterative approach is essential to guarantee that the final design achieves optimal functionality and reliability. Consequently, the production of one-of-a-kind prototypes and customizations is necessary to achieve the optimal performance of the sensor. Given the demanding specifications regarding the force-related deformation behavior and the durability of the components, only metals can be considered as the material for the sensor construction. The combination of these requirements makes it the ideal application area for metal additive manufacturing.

This novel approach to manufacturing enables the fabrication of intricate and bespoke metal components that align with the specific demands of each application [10]. In the context of metal printing, there are numerous approaches, including but not limited to direct metal laser sintering (DMLS) [11], laser powder bed fusion (LPBF) [12], electron beam melting (EBM) [13], and binder jetting (BJ) [14], which all utilize metallic powder as a feedstock. Furthermore, metal components can also be manufactured using material extrusion (MEX) [15], also known as fused deposition modeling (FDM), of a specialized metal-loaded filament [16, 17].

The objective of this study is to investigate the deformation bodies produced by additive manufacturing using LPBF and MEX technologies and to compare them with industry standard CNC machined parts. To ensure comparability of the produced parts, the same material type, 316L stainless steel, is defined for all manufacturing types. The manufactured components are subjected to functional and durability testing. In addition to the physical tests, a finite element method (FEM) simulation is employed to predict the functional properties of the specimens. In conclusion, the results pretraining to sensing applications are discussed.

II. Material and methods

The principal objective of this study is an innovative belt force sensor developed by the Biomechatronics Research Laboratory at FH Münster. This sensor is designed to accurately measure forces applied to various forms of belts, including those utilized in rehabilitation settings, such as orthosis and scoliosis corsets. In contrast to traditional methods, the sensor allows for the non-destructive measurement of forces on a belt, offering a valuable tool for monitoring and analysis, including the standardization of clamping devices to a test bench and the measurement of forces in daily life.

The operational methodology of the adaptable belt force sensor, as shown in Fig. 1, is predicated upon the conversion of the force exerted by the belt into a moment over a deflection bracket. The deformation body is composed of two identical L-shaped components that are joined together with the deflection bracket situated in the center. The belt is guided over the deformation body and through the deflection bracket, as illustrated in Fig. 1. One advantage of this operating principle is that the belt is not split or otherwise damaged for the measurement. By adjusting the width of the deformation body to a specific belt, it is possible to adapt the sensor to each specific use case.

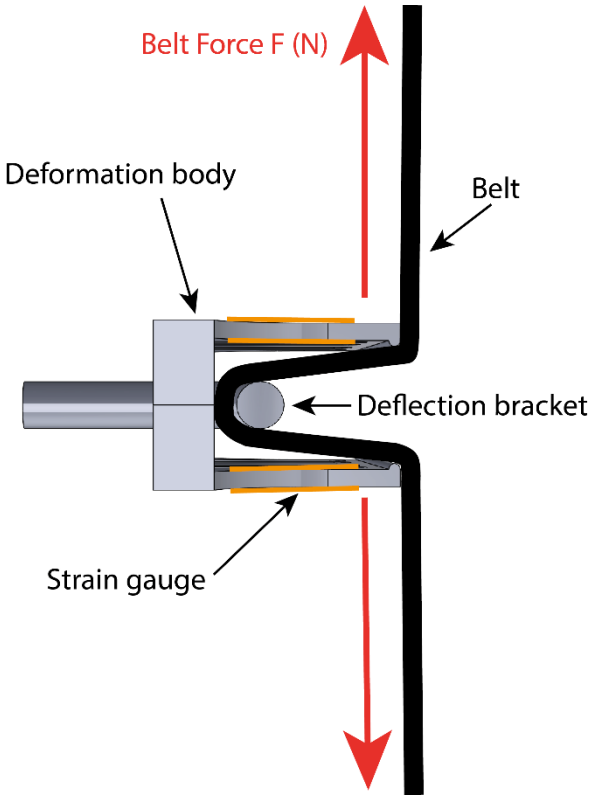

Figure 1: Schematic operating principle of the belt force sensor

Infinite Science Publishing

In this study, the strain gauges of the type 6/350 LY41, manufactured by Hottinger Brüel & Kjaer GmbH, were utilized for detecting the force applied to the deformation body. The strain gauges were affixed to both sides of each deformation body. The strain gauges exhibited an electrical resistance of 350 Ω ± 0.3%. The selected type of strain gauge was chosen due to its ready availability and its particular suitability for stress analysis. It was provided for use in educational and research activities. The formation of a Wheatstone bridge is possible by applying four strain gauges in total per sensor and connect them as shown in Fig. 2.

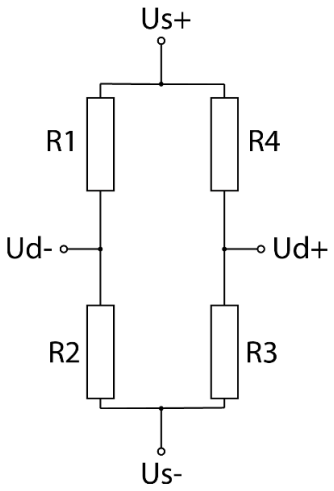

Figure 2. Schematic of the Wheatstone bridge connections

The force applied to the deformation body can be calculated over the bending moment from the measured strain. The maximum stress σ_b on the edge fiber is a result of the bending moment M_b and the moment of resistance W_b against bending as in (1).

$$\sigma_b = \frac{M_b}{W_b}. \tag{1}$$

For rectangular cross-sections with a beam width of b and a beam height of h, (2) applies.

$$W_b = \frac{bh^2}{6} \tag{2}$$

Using Hook`s law (3):

$$\sigma = E \times \epsilon \tag{3}$$

and equations (1) and (2), the moment from the measured strain on the surface of a bending beam with a rectangular cross-section is calculated through (4):

$$M_b = \epsilon \times E \times \frac{bh^2}{6}. \tag{4}$$

The combination of the linearized Wheatstone bridge equation (5) [19]:

$$\frac{\Delta Ud}{Us} = \frac{1}{4} \times \left(\frac{\Delta R_1}{R_1} - \frac{\Delta R_2}{R_2} + \frac{\Delta R_3}{R_3} - \frac{\Delta R_4}{R_4}\right) \tag{5}$$

and the strain-change in resistance relationship for the strain gauges (6) [19]:

$$\frac{\Delta R}{R} = k \times \epsilon \tag{6}$$

results in the bridge signal equation for a full bridge with four strain gauges in (7) [19]:

$$\frac{\Delta Ud}{Us} = \frac{1}{4}(4k\varepsilon) = k \times \epsilon. \tag{7}$$

Substitution of equation (7) into equation (4) provides the final formula, which is equation (8) [19]:

$$M_b = \frac{\Delta Ud}{Us} \times \frac{1}{k} \times E \times \frac{bh^2}{6} \tag{8}$$

In this study, the strain gauges utilized have a k-factor of approximately 2, and the E-module of the 316L stainless steel is 200 kN/mm², which results in a theoretical translation of (9)[20]:

$$500\frac{\mu m}{m} \triangleq 1\frac{mV}{V}. \tag{9}$$

The application of strain gauges to the deformation body is a manual process that may potentially influence the translation of the force into an electric signal. To ensure accurate measurement, the sensors are calibrated in a test bench. The calibration setup is depicted in Fig. 3. It consists of a solid frame constructed from aluminum profiles, and a stepper motor ARM911AC manufactured by Oriental Motor Co., Ltd. The motor is attached with a gearbox and spindle form ZIMM GmbH, which drives a cantilever arm over linear bearings. The applied force is quantified via the use of a load cell, (model K6D68) from M.E. Meßsysteme GmbH. This device is a six-component detector that is capable of measuring forces up to 1 kN and moments up to 100 Nm. The belt with the attached sensor is then affixed between the cantilever arm and the load cell. In order to perform the calibration process, the belt and the analog sensor are loaded with a target force, and the resulting signal is then detected using a universal measuring amplifier (QuantumX MX840B) from Hottinger Brüel & Kjaer GmbH.

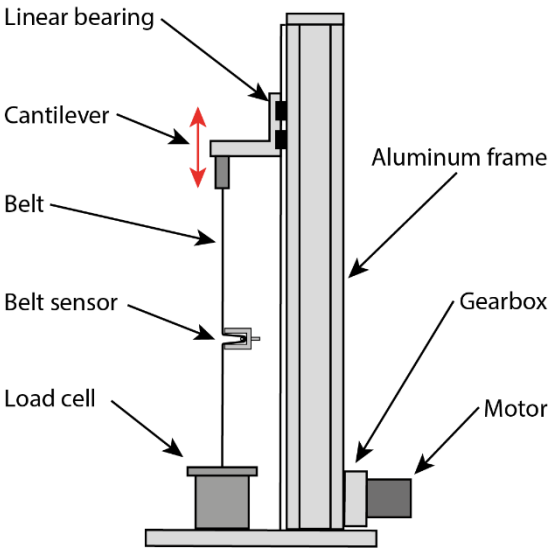

Figure 3: Schematic belt sensor calibration set-up using a vertical force test bench

It was determined that the traditional manufacturing processes were not suitable for producing customised components, resulting in the selection of CNC milling as the most appropriate solution. Nevertheless, additive manufacturing is demonstrated to be a more suitable and efficient method for the production of bespoke components. Laser powder bed fusion (LPBF) of metals was selected as the industry standard for the manufacture of metal components. This technology employs high-power lasers to fuse metal powder into a solid object, resulting in a production system that is both costly and energy-intensive. The LPBF printer was provided by the Laboratory for Machine Tools and Production Engineering. In contrast, MEX metal printing, which employs metal-loaded filaments and is compatible with any desktop printer, represents a more cost-effective alternative for the production of solid metal parts. The MEX printer was provided by the Biomechatronics Research Laboratory. The selection of both the additive manufacturing processes and the printers was based on their availability at FH Münster.

II.I. Manufacturing of the metal MEX specimen

The fabrication of solid metal components via the metal MEX printing technique represents a distinctive form of filament printing, wherein a specialized metal-loaded filament is used [17]. Following this, the filament undergoes conventional FDM printing, with adjustments to parameters such as temperature, speed etc. being made in order to align them with the desired material values. Once the print has been completed, the resulting parts must undergo a two-stage post-processing procedure, as shown in Fig. 4, in order to achieve the desired metal parts.

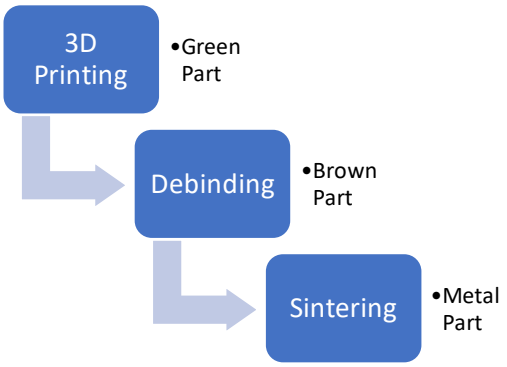

Figure 4: Schematic of the metal 3D printing processing steps

A spool of Ultrafuse 316L from BASF 3D Printing Solution GmbH was procured for the production of the MEX sample. The composition of this material is approximately 88 wt% 316L stainless steel particles with a size of 30-50 µm and approximately 12 wt% polyformaldehyde (POM) polymer binder matrix. The binder matrix is composed of a variety of polymers, including polypropylene (PP), dioctyl phthalate (DOP), dibutyl phthalate (DBP), and zinc oxide (ZnO) [18]. The specific composition of the matrix is being kept confidential by BASF.

BASF claims that the material can be printed on any standard desktop FDM-based printer. In this study, the Creatbot F430 desktop FDM printer was used for the printing of the samples. The printer is an enclosed core-XY FDM printer with a dual extruder print head. The entire build chamber can be actively heated to a maximum temperature of 70°C, while the 400 mm x 300 mm print bed can reach a maximum temperature of 120°C. Two distinct hotends are integrated into the printhead. One is designed for printing standard 3D printing materials, such as polylactic acid (PLA) or acrylonitrile butadiene styrene (ABS), which can reach temperatures of up to 260°C. The other hotend is equipped with a hardened steel nozzle and can reach temperatures of up to 420°C, allowing for the printing of abrasive and special filaments such as polyetheretherketone (PEEK) or carbon and glass-fiber reinforced filaments. BASF has published a design guideline for their Ultrafuse filament, which provides instructions for the printing process and other recommendations. The parameters utilized for the printing of the specimen are presented in Table 1. In order to enhance the adhesion of the specimen to the print bed, it was applied with a thin layer of Dimafix® adhesive spray and a 5 mm brim was set in the slicing software.

Table 1: Printing parameters for the Ultrafuse 316L specimen

Parameter	Value
Nozzle size	0.4 mm
Extrusion width	0.4 mm
Layer height	0.2 mm
Outlines	3
Infill	100 % rectilinear
Nozzle temperature	245 °C
Bed temperature	100 °C
Print speed	30 mm/s
Cooling	None

Following the printing process, the specimen was transferred to a service provider licensed by BASF for the catalytic debinding and sintering steps. Catalytic debinding is a thermochemical process that removes a portion of the binder matrix by exposing the printed parts to gaseous nitric acid (HNO3 > 98 %) in a nitrogen atmosphere at a temperature of 120°C. The duration of this step is contingent upon the thickness of the printed part and is concluded when a minimal debinding loss of 10.5% is achieved. Subsequently, the part is designated as the brown part. The remaining polymer binder serves as the requisite stabilizing element for the sintering process [22].

In the sintering step, the brown part undergoes a gradual thermal process in which the remaining binder is burned and the 316L stainless steel particles are fused into a solid metal part. The thermal process is divided into two phases and takes place in a hydrogen atmosphere to prevent oxidation and other detrimental processes.

In the initial phase, the component is elevated from ambient temperature to 600 °C at a rate of 5 K/min and maintained for one hour. Subsequently, the specimen is heated to 1380 °C by the same rate and held for three hours for the second phase, after which the furnace is cooled to room temperature. The removal of binder polymers will result in a shrinkage of approximately 20% in the X and Y directions and approximately 26% in the Z direction. This must be taken into consideration when preparing the print file. It is necessary to ensure that the printed part is oversized in order to meet the dimensional requirements following debinding and sintering [18].

The material composition for the sintered parts according to the material datasheet from BASF are shown in Table 2.

Table 2: Typical composition in % after sintering referring the BASF material datasheet []

C	Cr	Ni	Mn	Mo	Si	Fe
≤ 0.03	16-18	10-14	≤ 2	2-3	≤ 1	Balance

The sintered sensor components obtained from the service debinding and sintering process are shown in Fig. 5. In order to apply the strain gauges, the surface must be polished in order to achieve a better adhesion. Consequently, the 3D-printed parts were subjected to a glass bead blasting process.

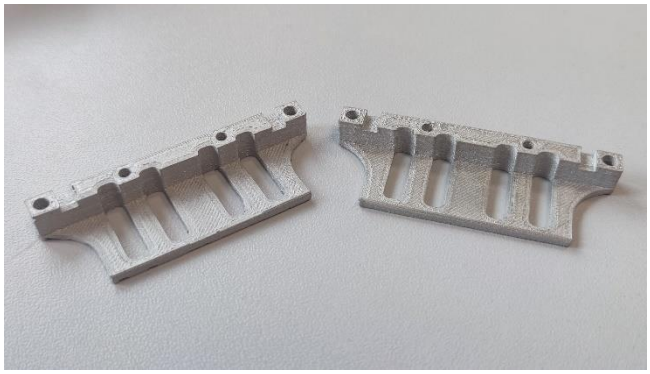

Figure 5: Metal MEX manufactured sensor parts after the sintering process

In order to form a complete sensor, the strain gauges were fitted and soldered in accordance with the previously described connection. Subsequently, the conductivity and resistance of each connection was verified using a multimeter to ensure that no faults had occurred.

II.II. Manufacturing of the LPBF specimen

The LPBF specimens were manufactured through a process that uses a high-power laser beam to selectively melt and fuse metallic powders layer by layer. In the initial phase of the printing process, the parts are fused to the build plate through the use of support structures. Once the printing process is complete, the residual powder must be removed by a suction system. The residual powder is then sieved and can be reused in the subsequent print job. Consequently, the printed parts must be detached from the support structure and the build plate using a band saw.

The 316L stainless steel powder used as material in this study has a volume equivalent diameter of d_{10} = 18.3 µm, d_{50} = 26.2 µm, and d_{90} = 37.5 µm. The chemical composition of the powder, as provided by the distributor, is detailed in Table 3. The specimens were manufactured using a LASERTEC 30 SLM 2nd Generation machine from DMG MORI, which has a build space of 300 x 300 x 300 mm. The inert gas Argon 4.6 was used, with a target gas flow rate of 1050 l/min. According to a previous study the laser focus diameter was maintained at 70 µm for all components, with a hatch distance of 90 µm. The oxygen level was maintained at 0.2 ± 0.05 vol.-%, and the layer thickness was set at 50 µm. The melting process was conducted in accordance with a 12 mm stripe pattern with a 31° layer rotation. The laser power was maintained at 254 W, and the scanning speed was set at 1000 mm/s. [23].

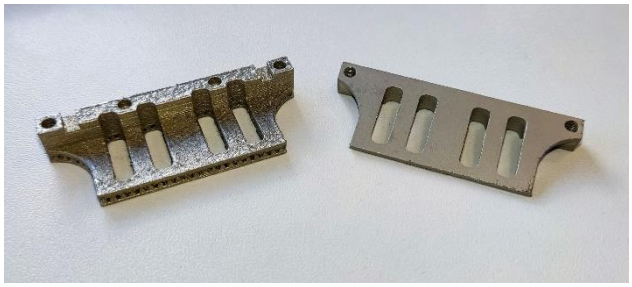

Figure 6: LPBF printed sensor parts as-built (left) and after glass bead blasting (right)

No post-process heat treatment was applied, thus allowing for an assessment of the as-built condition. In order to apply the strain gauges, the surface of the sensor parts was also subjected to glass bead blasting as shown in Fig 6.

II.III. Manufacturing of the conventional specimen

The reference specimen was manufactured using computer numerical control (CNC) milling technology. In order to achieve an industrial-grade part, the manufacturing process was outsourced to a service provider. The 3D model and material specifications were identical to those used for the additive manufacturing process. The chemical composition of the material used for the conventional components is presented in Table 4.

The milled parts did not require any surface treatment or other post-processing. The specimens were provided with a clean and smooth surface that was suitable for the strain gauge instrumentation. The service manufactured parts are shown in Fig. 7.

Figure 7: CNC milled industrial grade sensor parts made of 316L stainless steel

After the application of the strain gauges the completed sensor is shown in Fig. 8.

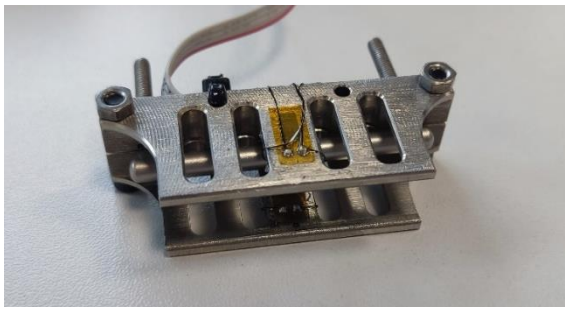

Figure 8: Complete instrumented CNC milled sensor with strain gauges and soldered connectors

II.IV. Comparison of the mechanical properties

The mechanical properties of the materials used in this study vary greatly depending on the processing method. Fig. 9 shows a comparison of the value's tensile strength and yield strength for all three manufacturing processes. The data for the MEX sample was obtained from the material datasheet provided by BASF.

Table 3: Chemical composition of the 316L powder according to the distributor

	C	Cr	Ni	Mn	Mo	Si	Fe	P	S	Cu	N	O
Min.	-	16.0	10.0	-	2.0	-	-	-	-	-	-	-
Max.	0.03	18.0	14.0	2.00	3.0	0.75	Bal	0.045	0.015	0.75	0.1	0.1
Result	0.02	17.9	12.9	1.24	2.3	0.70	Bal	0.014	0.004	0.05	0.1	< 0.1

Table 4: Chemical composition of the 316L material used for conventional manufacturing according to the service provider

	C	Cr	Ni	Mn	Mo	Si	P	S	N
Min.	-	16.5	10.0	-	2.0	-	-	-	-
Max.	0.03	18.5	13.0	2.0	2.5	1.0	0.045	0.030	0.1

The mechanical properties of the LPBF-manufactured 316L stainless steel were not provided with sufficient accuracy by the material distributor. Consequently, the material properties were obtained through tensile testing which was conducted in accordance with the specifications outlined in DIN EN ISO 6892-1 method B.

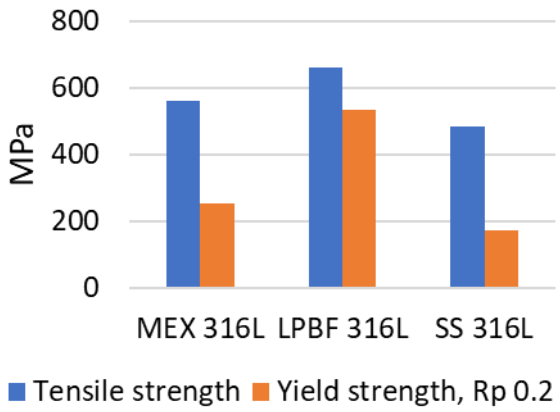

Figure 9: Comparison of tensile strength and yield strength of the different processed 316L stainless steel

A total of five round tensile specimens with threads (Form B) were subjected to testing. The specimens were constructed in accordance with the dimensions specified in DIN 50125, with a diameter d_0 of 5 mm and a length L_0 of 25 mm. The testing was performed on a universal testing machine, specifically the AllroundLine 100 kN machine from Zwick Roell.

As shown in Fig. 9, both additive manufactured samples exhibited higher tensile strength and yield strength than the conventional material values. The LPBF sample exhibited approximately three times the yield strength value of the conventional AISI 316L stainless steel and twice the yield strength of the MEX sample. This distinction can be attributed to the superior microstructure that can be attained through the LPBF technique; a quality that has been previously described by Liverani et al. [21].

In contrast to the tensile strength, the MEX printed sample exhibited the highest values at elongation at break, with a percentage exceeding 50%. Consequently, the LPBF sample exhibited comparable values to those observed in

the conventional sample. This also indicates that the more resilient microstructure is not associated with a loss of ductility.

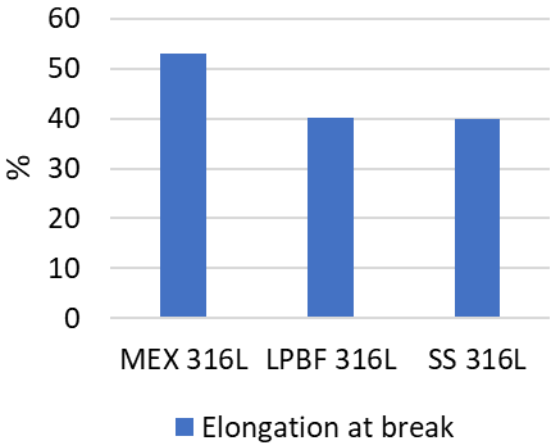

Figure 10: Comparison of the elongation at break for the different processed 316L stainless steel samples

II.V. FEM simulation

A finite element (FEM) simulation model of the loading condition is created based on the mechanical properties described in the preceding section. The objective of this simulation is to predict the critical load level at which plastic deformation occurs. Furthermore, if the simulation yields valid results, it can serve as a design and prediction tool for the creation and adoption of the sensor for new use cases.

The simulation was created using computer-aided design (CAD) software, specifically SolidWorks 2022, with the simulation add-on. Consequently, the three-dimensional model of a single sensor component is imported into the simulation add-on. The study design was set to a static loading scenario. The loading condition is adjusted by applying a fixation (see green indicators in Fig. 11) at the back and interface surface, as well as by applying a force (see purple arrows in Fig. 11) to the edge of the sensor.

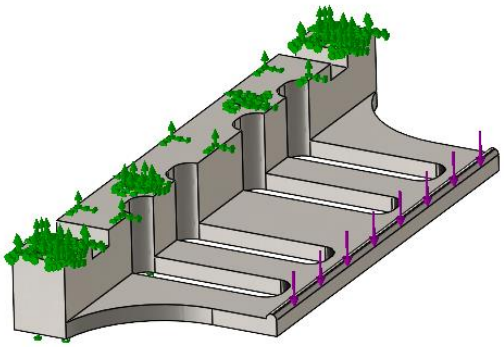

Figure 11: Schematic of the fixation (green indicators) and the applied force vector (purple arrows) of the FEM simulation model in SolidWorks 2022

In order to predict the individual critical loading, a separate material model was adopted for each processing method, with the material properties described in the preceding section. Due to the sensor design, both parts are loaded equally, which reduces the need for simulating the entire sensor and also reduces the complexity and the calculation time required.

II.VI. Functional and cyclic testing

The functional testing was conducted using a test bench that had been specifically designed for the purpose of enabling precise and slow testing conditions. Therefore, the sensor was applied to the belt, which was then clamped between the load cell and the cantilever. For the measurement of the electrical offset signal, the belt and the sensor were clamped unloaded, as shown in Fig. 12. Subsequently, the signal offset is adjusted, and the belt is tensioned until a force is registered by the load cell. To initiate the functional testing, the belt is slightly unloaded to begin at an unloaded condition. Once the measurement is initiated, the test bench will apply the set target force at a rate of 200 N/min to detect the loading signal. Once the target force has been reached, the force is reduced in order to detect the unloading signal. A test cycle is considered complete when the force level has returned to its initial state. The motion and control system of this setup has been optimized for high precision, allowing for meticulous evaluation of sensor functionality under controlled conditions. However, this emphasis on precision and slow movements renders the test bench unsuitable for cyclic testing which requires the capability to handle repetitive, high-speed load applications.

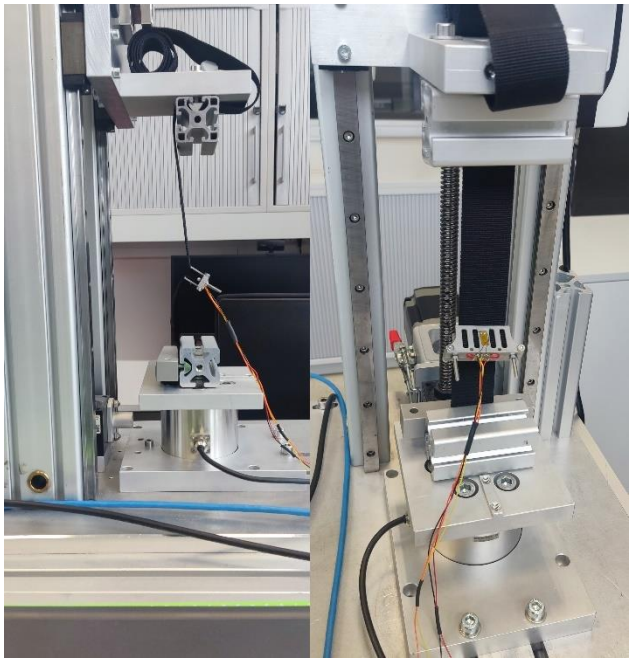

Figure 12: Functional and calibration test bench with belt and sensor clamped in an unloaded condition

To address the need for cyclic testing, a separate test bench was used. The secondary setup is equipped to perform repetitive loading and unloading cycles at higher speeds, which is essential for evaluating the durability and fatigue life of the sensors under conditions that mimic real-world operational stresses and is shown in Fig. 13 and 14. Therefore, the sensors will be subjected to a total of 50,000 loading cycles. The motion system of the test bench is comprised of two linear motors from NTI AG, LinMot & MagSpring. A KM30z load cell with a 1 kN range from ME-Meßsysteme GmbH is used for the force control, and the frame is constructed from solid aluminum profiles. The test bench is configured using the LinMot drive software, LinMotTalk, which enables a closed loop force control program to execute the loading and unloading cycles with the specified target force and target frequency of 1 Hz. To identify any changes in sensor response, functional interim measurements are conducted every 10,000 cycles with the functional test bench.

The use of two distinct test benches ensures that a comprehensive assessment of both functional performance and long-term reliability of the sensors can be carried out under appropriate testing environments.

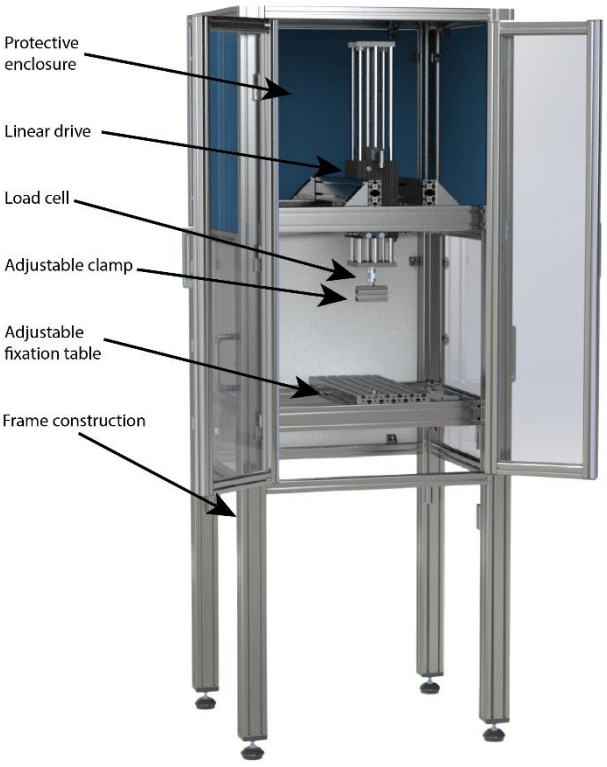

Figure 13: Schematic of the cyclic test bench for durability and fatigue life testing

Two sensor half units were manufactured to create a fully functional sensor. However, only a single complete sensor per manufacturing method was subjected to the aforementioned testing procedure.

This decision was made due to the prolonged testing duration during the cyclic testing phase and the objective of investigating a bespoke, single-purpose application sensor. Consequently, it was not feasible to investigate several specimens for each manufacturing method.

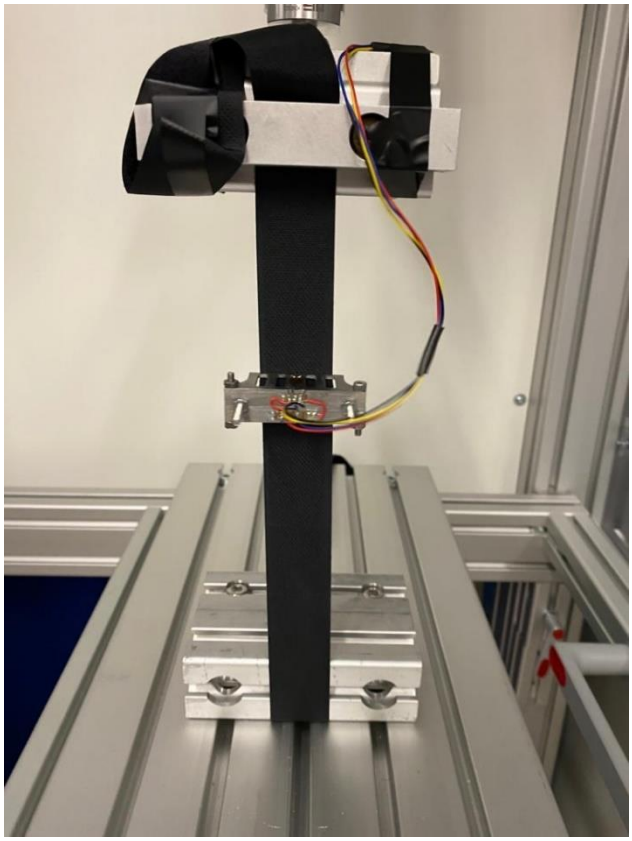

Figure 14: Sensor and belt fixed in the cyclic test bench for durability and fatigue life testing

III. Results and discussion

The following section presents the results of the actions previously described, starting with the findings from the FEM simulations, which were used to inform the design of both functional and cyclic tests. Detailed outcomes of the two-stage testing are provided, encompassing both the durability and fatigue life assessments. Additionally, an ultimate strength test was performed to evaluate the accuracy of the FEM simulation predictions.

III.I. FEM simulation

The FEM simulation was conducted with the objective of pretending the critical load level to ensure that the sensors would not be overstressed during functional and cyclic testing. The FEM simulation results, which include stress-strain analysis and deformation mappings, provide a comprehensive understanding of the mechanical behavior of the sensors manufactured through different methods. The results of the simulation are shown in Fig. 15.

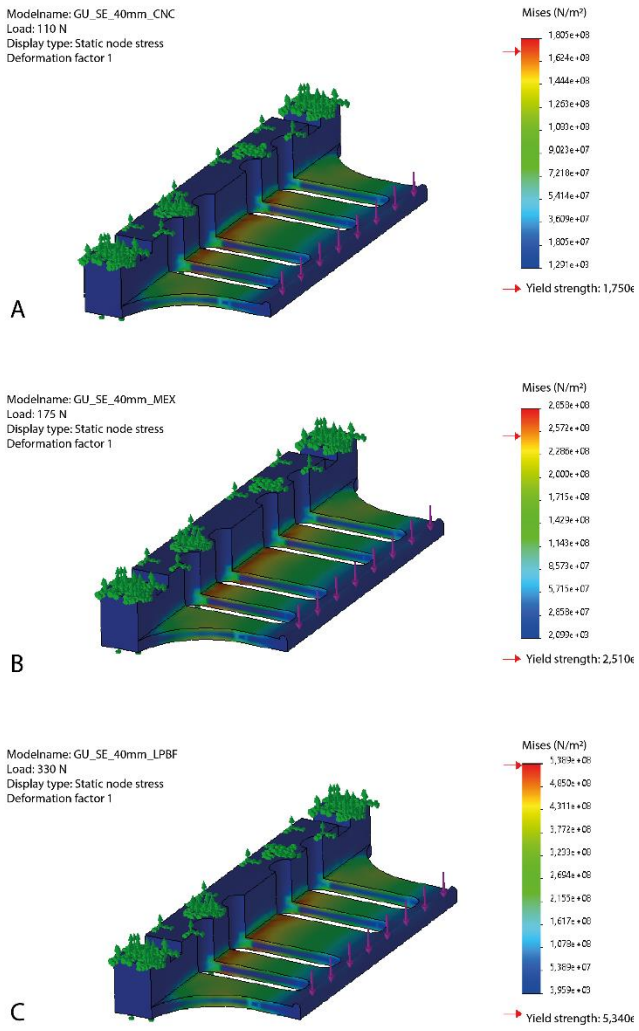

Figure 15: FEM simulation results for predicting the critical load level before entering plastic deformation for all manufactured sensor components

As shown in Fig. 15, the critical load level exhibits variability across the various manufactured sensor parts. Analogous to the material properties previously described, the conventionally manufactured sensor exhibits the lowest capable force of approximately 110 N until plastic deformation (see Fig. 15 A). For the MEX sensor, a critical force of 175 N was calculated (see Fig. 15 B). The LPBF-manufactured part exhibits the highest critical load level of approximately 330 N until plastic deformation (see Fig. 15 C). In addition to the disparate values observed in the stress-strain analysis, the deformation mapping for the distinct manufacturing methods exhibited a uniform behavior, with a stress accumulation occurring at the transition of the lever arm to the sensor's back part.

In order to ensure that no sensor will be overstressed during functional testing and to maintain consistent testing conditions for all specimens, the target force for functional testing was set to 100 N.

III.II. Functional testing

In order to conduct functional testing and sensor calibration, the vertical force test bench described in Fig. 3 was used. The target force of 100 N was set following the FEM simulation results. To ensure that the settling behavior would not produce any disorders, a total of five cycles were measured, with the first and last cycles excluded from the observation, which is shown in Fig. 16.

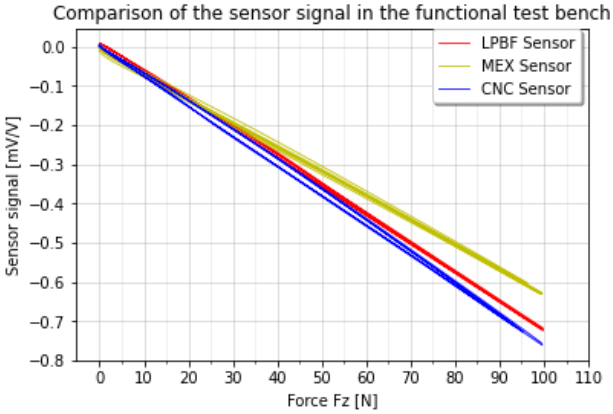

Figure 16: Sensor signal response during functional testing up to a force of 100 N

The sensor signals exhibited a similar linear response under both loading and unloading conditions, with only minor variations in the signal gradient. This consistent linear behavior between the loading and unloading phases indicates a low hysteresis loss, suggesting minimal energy dissipation and high accuracy in force detection. The investigation demonstrated that all three sensors were functional and effective in detecting belt forces.

III.III. Durability testing

Each sensor underwent durability and fatigue life testing on a cyclic testing bench. In order to ensure a safety margin below the critical load level, the target force was set at approximately 80% of the maximum capacity of the weakest sensor. This maximum capacity value was consistently applied to the other specimens as well, in order to ensure uniform testing conditions across all sensors. As shown in Fig. 17, the clamping device, along with the weight of the belt and sensor, results in a force offset of approximately 12.5 N.

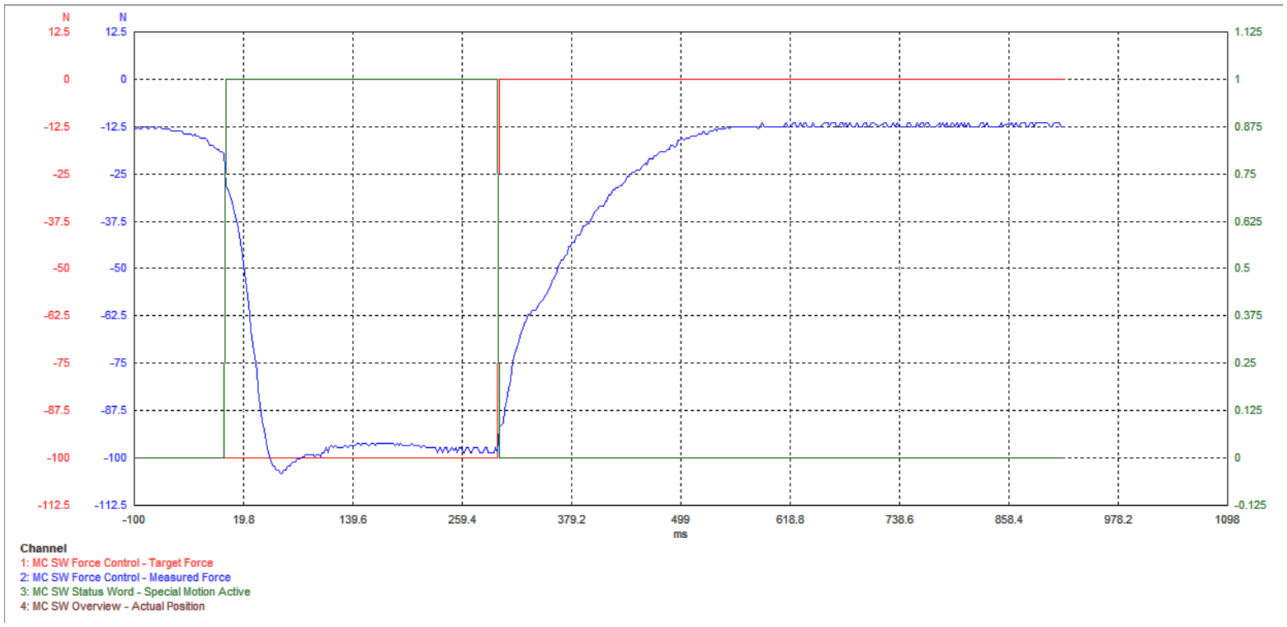

Figure 17: Example control loop of the loading and unloading during the cyclic testing

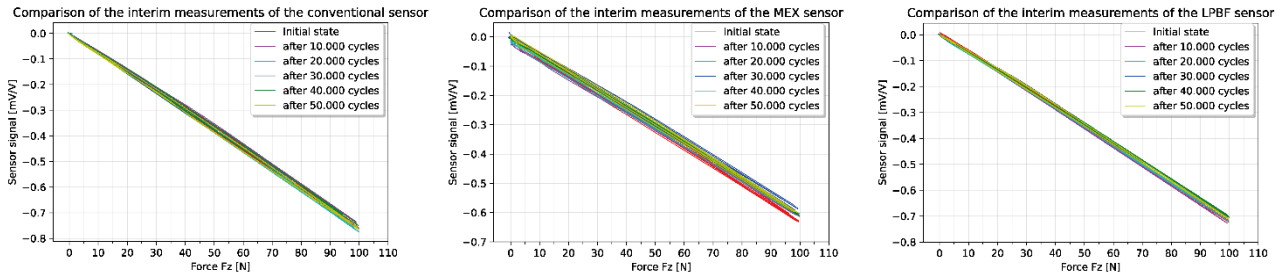

Figure 18: Comparison of every interim measurement for each sensor during the durability and fatigue life testing

To address this offset, the closed-loop force control system was programmed to achieve a total target force of 100 N, thereby compensating for the initial offset and ensuring accurate testing conditions.

As previously stated, an interim measurement was conducted following each 10,000 cycles during the cyclic testing. The results of the measurements for each sensor are shown in Fig. 18. The measurements demonstrate a consistent linear signal with minimal variations in the signal gradient across all sensors. The conventional and LPBF manufactured sensors exhibited minimal changes in their characteristics over the 50,000-cycle testing period. The MEX-printed sensor exhibited slightly more variation in characteristics which were also within the acceptable tolerances. The results of the durability and fatigue life testing indicate that all sensors have met the targeted performance criteria and can be considered durable for the intended application in real-world testing.

III.IV. Ultimate strength test

To validate the predictions made by the FEM simulations, ultimate strength testing was conducted on the manufactured sensors. The FEM simulations predicted that the strongest sensor, the LPBF manufactured, could withstand approximately 330 N before failure. To ensure failure during testing and thereby thoroughly assess the sensors' ultimate strength, the target force for the testing was set to 350 N. This approach provides a crucial comparison point for evaluating the accuracy of the FEM simulations by subjecting the sensors to loads slightly beyond the predicted maximum capacity.

The critical load for each sensor was identified by observing deviations in the sensor signal curve from its linear behavior, as shown in Fig. 19. For the conventionally manufactured specimen, a clear deviation from linearity began at a load of approximately 120 N, slightly higher than the simulation prediction of 110 N, indicating a marginally greater load capacity than anticipated.

In the case of the LPBF-manufactured specimen, the deviation was less pronounced compared to the conventional sensor. The critical load for this specimen was reached at approximately 320 N, which closely aligns with the FEM simulation prediction of 330 N.

For the MEX-printed specimen, the sensor signal showed almost no response to the load up to 110 N, followed by an

exponential deviation beyond this point. This significant deviation prompted the termination of the measurement at approximately 250 N to prevent potential damage to the test bench components. The MEX-printed sensor's behavior under load suggests a different failure mode compared to the other specimens. This suggests that the error is not primarily related to the mechanical properties of the sensor, but rather to a problem within the electrical connection or detachment of the strain gauges.

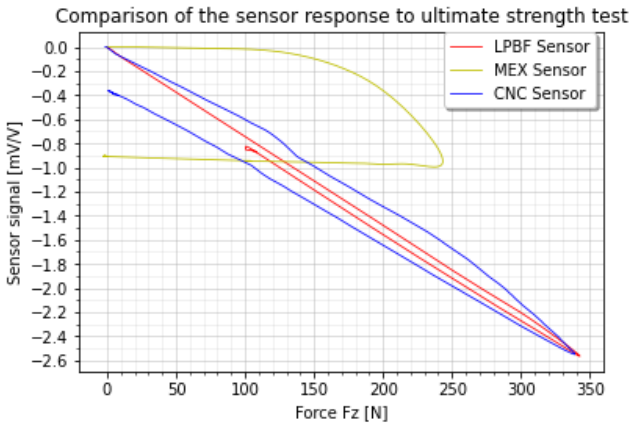

Figure 19: Comparison of the sensor response to the ultimate strength testing of all sensors

III.V. Discussion

This study aimed to evaluate the performance of force sensors manufactured using three different methods: LPBF and MEX additive manufacturing and conventional CNC machining. While the results provide valuable insights, several limitations and considerations need to be addressed to fully understand the implications of our findings.

Firstly, physical tests were only conducted on the LPBF samples in order to obtain the material properties which was not provided with sufficient accuracy by the distributor. For the conventional and MEX-printed samples, we relied on the material properties provided in the datasheets. No independent validation was performed to verify these properties. This reliance on datasheet information could introduce uncertainties, as actual material properties can vary due to factors such as manufacturing processes and batch differences. Future studies should include comprehensive physical testing on all samples to ensure accurate and reliable data of material properties.

Secondly, the FEM simulation was based on isotropic material models. Due to the constraints of the software used for the simulation, it was not possible to consider the anisotropic material behavior. It is often observed that MEX-printed components exhibit directional dependency in their mechanical properties, a consequence of the layer-by-layer deposition process. The failure to not consider this anisotropy in simulations can result in the generation of inaccurate predictions of sensor performance.

The incorporation of anisotropic material models into FEM simulations would result in a more accurate representation of the MEX-printed sensor's behavior under load. In order to ensure more accurate predictions, it is recommended that further investigations be conducted using a more accurate simulation software. This is particularly important when the results of the simulations are intended to serve as guidelines for the design of sensors.

During the functional testing, we observed an offset or slight difference in the signal gradient, which could be attributed to the placement of the strain gauges. The exact positioning and bonding quality of the strain gauges can significantly affect the sensor output. Ensuring precise and consistent placement of strain gauges is crucial for obtaining accurate and repeatable measurements. Further investigation into the optimal placement and attachment methods for strain gauges could help minimize these discrepancies. Nevertheless, the calibration process and the capacity to store the individual calibration curve on each sensor ensure that the accuracy of the sensor output is not affected by the placement of the strain gauges.

In the cyclic testing, we noted that the force regulation was not perfect due to limitations in the controller used. The cyclic testing requires precise control of loading and unloading forces to accurately simulate real-world conditions. However, the limitations of the controller resulted in slight deviations from the target force, which could affect the reliability of the fatigue life data. Upgrading to a more advanced control system with finer force regulation capabilities would enhance the accuracy of cyclic testing and provide more reliable data on sensor durability.

The ultimate strength testing, which served as a validation of the simulation predictions, yielded good results within an acceptable tolerance for the conventional and LPBF printed sensors. Conversely, the MEX-printed sensor exhibited minimal response up to 110 N, followed by an exponential deviation that necessitated the cessation of testing at 250 N to avoid damaging the test bench The observed behavior and signal responses differ markedly from those obtained during the cyclic testing. A comprehensive examination was unable to identify any discernible cause for this sudden change in sensor signal behavior. This indicates that the MEX-printed sensor may demonstrate distinctive electronic malfunction or failure mechanisms rather than material inconsistencies, which cannot be entirely excluded but would have resulted in a different sensor signal. Consequently, a definitive conclusion regarding the precision of the FEM prediction for the MEX sensor remains pending. It is noteworthy that the anisotropic mechanical behavior of the MEX-printed sensor, resulting from its layer-by-layer construction, was not incorporated into the simulation model.

The disparities in the mechanical properties between LPBF steel and the conventional product, which were already apparent in the comparison of material properties, are also reflected in the physical tests. This is due to the LPBF manufacturing process, which allows for optimized microstructures, resulting in enhanced mechanical characteristics, including increased tensile strength, hardness, and fatigue resistance.

Furthermore, the combination of heat induction through laser processing and rapid solidification rates in LPBF can refine the grain structure, thereby enhancing the material's strength and durability. To clarify the origin of these mechanical properties, microstructural analysis should be conducted in future investigations. Additionally, to equate any process-related heat influence, a comparable heat treatment should be applied to all specimens.

Nevertheless, the observed discrepancies in the MEX-printed sensor highlight the necessity for further enhancement of simulation models and supplementary physical testing. These steps are of paramount importance in order to fully validate FEM simulations as predictive tools for sensors produced by various manufacturing methods. Further investigations are required to accurately capture the anisotropic behavior of MEX-printed sensors in FEM simulations and to ensure comprehensive validation of sensor robustness across different fabrication techniques. However, due to the limited number of specimens, no general conclusion can be drawn regarding the validity of the simulation as a prediction tool. For this reason, further and more comprehensive testing is required.

In summary, while the study provides promising results regarding the performance of LPBF-manufactured sensors, several limitations need to be addressed in future research. Comprehensive physical testing of all samples, consideration of anisotropic material properties in simulations, precise strain gauge placement, and improved force control in cyclic testing are essential steps to enhance the reliability and validity of the findings. Addressing these aspects will lead to a more thorough understanding of the performance and suitability of different manufacturing methods for producing reliable force sensors.

IV. Conclusions

This study undertook a comprehensive evaluation of the performance of force sensors manufactured through three distinct methods: conventional CNC machining, LPBF, and MEX 3D printing. A combination of FEM simulations, functional testing, durability assessments and ultimate strength testing was employed to demonstrate the potential of additive manufacturing methods for sensing technology applications.

The results of the FEM simulations provided a preliminary framework for predictive analysis, particularly for LPBF and conventionally manufactured sensors, where the simulation predictions closely matched the experimental outcomes. In contrast, the MEX-printed sensors exhibited significant deviations observed during ultimate strength testing. A subsequent in-depth review highlighted the need for more comprehensive modeling approaches that account for the unique material characteristics and failure mechanisms.

The functional testing confirmed the operational capability of all sensors and their suitability for the intended application. Furthermore, all sensors demonstrated the ability to withstand 50,000 cycles of cyclic testing, thereby confirming their reliability and durability, as well as their fatigue life performance. The characteristics of the LPBF-printed material also demonstrated an increasing strength of nearly three times compared to the conventional method. These advantages offer the potential for more creative design of sensor parts and the expansion of the application field to include higher-loaded use cases.

Acknowledgments

Research funding: The authors state no funding involved.

Author's statement

Conflict of interest: Authors state no conflict of interest. Informed consent has been obtained from all individuals included in this study.

References

[1] A. Aimar, A. Palermo, B. Innocenti (2019), The role of 3D printing in medical applications: a state of the art, J Healthc Eng, 2019, pp. 1-10, 10.1155/2019/5340616, In press.
[2] Ventola CL. (2014) Medical Applications for 3D Printing: Current and Projected Uses. P T. 2014 Oct;39(10):704-11. PMID: 25336867; PMCID: PMC4189697.
[3] Berman, B. (2012). 3-D printing: The new industrial revolution. Business Horizons, 55(2), 155–162 DOI: 10.1016/j.bushor.2011.11.003
[4] Lin, D., et al. (2014). Three-dimensional printing of complex structures: man made or toward nature? ACS Nanotechnology, 8. DOI: 10.1021/nn504894j
[5] Morrison, Robert J., et al. "Regulatory considerations in the design and manufacturing of implantable 3D-printed medical devices." Clinical and translational science 8.5 (2015): 594-600.
[6] Mohseni, M.; Hutmacher, D.W.; Castro, N.J. Independent Evaluation of Medical-Grade Bioresorbable Filaments for Fused Deposition Modelling/Fused Filament Fabrication of Tissue Engineered Constructs. Polymers 2018, 10, 40. DOI: 10.3390/polym10010040
[7] Agnieszka Haryńska, et al., A comprehensive evaluation of flexible FDM/FFF 3D printing filament as a potential material in medical application, European Polymer Journal, Volume 138, 2020, 109958, ISSN 0014-3057, https://doi.org/10.1016/j.eurpolymj.2020.109958.
[8] Han, T.; Kundu, S.; Nag, A.; Xu, Y. 3D Printed Sensors for Biomedical Applications: A Review. Sensors 2019, 19, 1706. DOI: 10.3390/s19071706
[9] Stefano, J. S., et al. (2022). Electrochemical (Bio)sensors enabled by fused deposition modeling-based 3d printing: a guide to selecting designs, printing parameters, and post-treatment protocols. Analytical Chemistry, 94(17), 6417–6429. DOI: 10.1021/acs.analchem.1c05523
[10] Banks, "Adding Value in Additive Manufacturing: Researchers in the United Kingdom and Europe Look to 3D Printing for Customization," in IEEE Pulse, vol. 4, no. 6, pp. 22-26, Nov. 2013, doi: 10.1109/MPUL.2013.2279617
[11] Syed A.M. et al., Additive manufacturing: scientific and technological challenges, market uptake and opportunities, Materials Today, Volume 21, Issue 1, 2018, Pages 22-37, ISSN 1369-7021, https://doi.org/10.1016/j.mattod.2017.07.001.
[12] I. Gibson, D.W. Rosen, and B. Stucker, Additive Manufacturing Technologies: Rapid Prototyping to Direct Digital Manufacturing (Berlin: Springer, 2009)

[13] Li Y, Kan W, Zhang Y, Li M, Liang X, Yu Y, Lin F (2021) Microstructure, mechanical properties and strengthening mechanisms of IN738LC alloy produced by Electron Beam Selective Melting. Addit Manuf 47:102371
[14] Sauerbrunn, E., Chen, Y., Didion, J., Yu, M., Smela, E., & Bruck, H. (2015). Thermal imaging using polymer nanocomposite temperature sensors. Physica Status Solidi, (a):212. DOI: 10.1002/ pssa. 201532114
[15] Sharafi S, Santare MH, Gerdes J, Advani SG (2021) A review of factors that influence the fracture toughness of extrusion-based additively manufactured polymer and polymer composites. Addit Manuf 38:101830
[16] Jiang D, Ning F (2021) Additive manufacturing of 316L stainless steel by a printing-debinding-sintering method: effects of microstructure on fatigue property. J Manuf Sci E-T Asme 143(9):1–30
[17] Safka J, Ackermann M, Machacek J, Seidl M, Vele F, Truxova V (2020) Fabrication rocess and basic material properties of the basf Ultrafuse 316Lx material. Mm Sci J 2020:4216–4222
[18] Bin Liu, Yuxiang Wang, Ziwei Lin, Tao Zhang, Creating metal parts by Fused Deposition Modeling and Sintering, Materials Letters, Volume 263, 2020, https://doi.org/10.1016/j.matlet.2019.127252.
[19] ME-Meßsysteme GmbH, Basics of bridge circuit, https://www.me-systeme.de/en/technology-first/strain-gauge/basics-of-bridge-circuit, Accessed 25 May 2024.
[20] Hottinger Brüel & Kjaer GmbH, Datasheet of typ LY41-6/350 strain gauges, https://www.hbm.com/fileadmin/mediapool/hbmdoc/technical/S01265.pdf, Accessed 25 May 2024.
[21] Liverani, E., Toschi, S., Ceschini, L. and Fortunato, A. (2017), “Effect of selective laser melting (SLM) process parameters on microstructure and mechanical properties of 316L austenitic stainless steel”, Journal of Materials Processing Technology, Vol. 249, pp. 255-263.
[22] BASF Process Instructions Ultrafuse 316L, information on: https://forward-am.com/wp-content/uploads/2021/01/Process-Instructions-Ultrafuse-316L.pdf
[23] Berghaus, M., Florian, S., Solanki, K. et al. Effect of high laser scanning speed on microstructure and mechanical properties of additively manufactured 316L. Prog Addit Manuf (2024). DOI: 10.1007/s40964-024-00693-y